Self-assembly of pulverized nanoparticles: an approach to realize large-capacity, long-lasting, and ultrafast-chargeable Na-ion batteries

Journal:	*Nano Letters*
Manuscript ID	nl-2021-02518r.R4
Manuscript Type:	Communication
Date Submitted by the Author:	23-Oct-2021
Complete List of Authors:	Park, Jun-Hyoung; Korea University, Material sci. & eng. Choi, Yong-Seok; University College London, Department of Chemistry Kim, ChangHyeon; Gyeongsang National University, Department of Materials Engineering and Convergence Technology Byeon, Young-Woon; Lawrence Berkeley National Laboratory, Materials Sciences Division Kim, Yongmin; Pohang University of Science and Technology, Center for Advanced Aerospace Materials Lee, Byeong-Joo; Pohang University of Science and Technology, Ahn, Jae-pyoung; Korea Institute of Science and Technology, Nano Materials Analysis Center Ahn, Hyojun; Gyeongsang National University, School of Materials Science and Engineering Lee, Jae-Chul; Korea University, Department of Materials Science and Engineering

SCHOLARONE™
Manuscripts

Self-assembly of pulverized nanoparticles: an approach to realize large-capacity, long-lasting, and ultrafast-chargeable Na-ion batteries

Jun-Hyoung Park[1,†], Yong-Seok Choi[1,2,†], ChangHyeon Kim[3], Young-Woon Byeon[1,4], Yongmin Kim[5], Byeong-Joo Lee[5], Jae-Pyoung Ahn[6], Hyojun Ahn[3,*], Jae-Chul Lee[1, *]

[1]Department of Materials Science and Engineering, Korea University, Seoul 02841, South Korea

[2]Department of Chemistry, University College London, 20 Gordon Street, London WC1H 0AJ, UK

[3]Department of Materials Engineering and Convergence Technology, Gyeongsang National University, Jinju 52828, South Korea

[4]Materials Sciences Division, Lawrence Berkeley National Laboratory, Berkeley CA 94720, United States

[5]Center for Advanced Aerospace Materials, Pohang University of Science and Technology, Pohang 37673, South Korea

[6]Advanced Analysis Center, Korea Institute of Science and Technology, Seoul 02792, South Korea

TOC graphic:
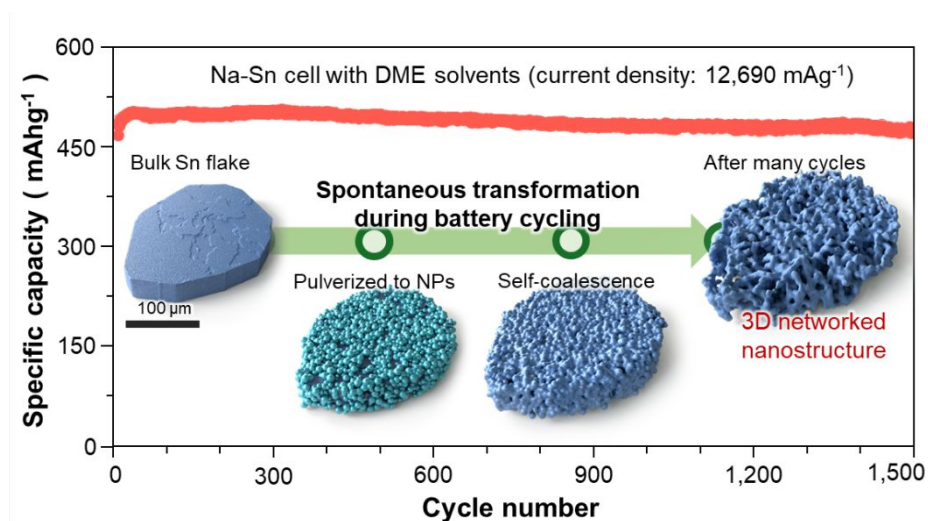
Abstract: The fabrication of battery anodes simultaneously exhibiting large capacity, fast charging capability, and high cyclic stability is challenging because these properties are mutually contrasting in nature. Here, we report a rational strategy to design anodes outperforming the current anodes by simultaneous provision of the above characteristics without utilizing nanomaterials and surface modifications. This is achieved by promoting spontaneous structural evolution of coarse Sn particles to three-dimensionally networked nanostructures during battery cycling in an appropriate electrolyte. The anode steadily exhibits large capacity ($\sim$480 mAhg^{-1}) and energy retention capability (99.9%) during >1,500 cycles even at an ultrafast charging rate of 12,690 mAg^{-1} (15C). The structural and chemical origins of the measured properties are explained using multi-scale simulations combining molecular dynamics and density functional theory calculations. The developed method is simple, scalable, and expandable to other systems and provides an alternative robust route to obtain nanostructured anode materials in large quantities.

Keywords: ultrafast charging, stress-induced dislocation, dislocation pipe diffusion, pulverization, self-assembly

†These authors contributed equally to this work.

*To whom correspondence should be addressed: Hyojun Ahn (email: ahj@gnu.ac.kr),

Jae-Chul Lee (email: jclee001@korea.ac.kr)

In alloying anodes, the charging and discharging are always accompanied by large volume changes associated with the repetitive insertion and extraction of carrier ions. This unavoidable volumetric change necessarily develops stresses at the propagating interface and causes pulverization/fragmentation of anode materials[1-3]. Until recently, this behavior was considered detrimental and undesirable for most battery systems, because it leads to structural degradation and reduces the associated rate performance, cyclic stability, and capacity of the anode[2-6]. However, for certain systems and in the presence of an appropriate electrolyte, this seemingly destructive process can be useful to construct porous nanostructure, which is crucial to fabricate anodes having simultaneously improved capacities, rate performances, and cyclabilities.

Nanoparticles (NPs) are prone to spontaneous coalescence in appropriate solutions[7-10], and thus can often reconfigure to a porous three-dimensional (3D) nanostructure consisting of NPs. When such reorganization occurs in an anode material, the resultant structural architecture can transport carrier ions through surfaces and grain boundaries at faster rates[11, 12], which improves the rate performance of the battery. Furthermore, during battery cycling, these porous nanostructures can sustain large volumetric changes, which increases the capacity and cyclic stability of the anode. In this regard, the coalescence of NPs can be used as a basic strategy to develop ultrafast-chargeable batteries with large capacities and cyclic stability. However, to utilize these properties provided by the coalescence of NPs, it is essential to develop an effective method to obtain the required NPs for the subsequent coalescence process. One approach to promote the two individual events in a sequential order is the use of low-yielding and low-melting metals. For low-yielding metals, the insertion of carrier ions often proceeds with the generation of dislocations in front of the advancing interface[13, 14]. Thus-formed

3 / 23

dislocations act as preferential pathways for ionic diffusion, transforming the initially coarse-grained bulk metal into a nanograined one[13]. During the subsequent charging stage, the extraction of carrier ions destroys the bulk metal into NPs. In appropriate liquid media, pulverized NPs, particularly those with low melting temperatures, can spontaneously coalesce even at ambient temperature and yield porous nanostructures[7-9]. In this context, Sn, owing to its low yield strength and melting temperature[15], is expected to act as an ideal testbed material for the fabrication of self-assembled nanostructured anodes using pulverized NPs.

In this study, using a Na–Sn battery system, we design anodes for Na-ion batteries that outperform the current anodes by simultaneous provision of large capacity, fast charging capability, and long cycling lifetime without using surface modifications. We experimentally confirm the above concept for the fabrication of an anode material that can operate at ultrafast rates without reducing the capacity over an extended battery cycling. At a current rate of 12,690 mAg^{-1} (equivalent to $15C$), the fabricated anode with self-assembled Sn nanostructures stored ~480 $mAhg^{-1}$ without modifications, which lasts during >1,500 (red dashed line in Figure S1) with 99.9% of energy retention. To explore the mechanism of the observed structural evolution and associated electrochemical properties, this study addresses four fundamental issues. 1) By observing the generation of dislocations in bulk Sn crystals and associated dislocation-pipe diffusion of Na during sodiation, we clarified the restructuring process of the bulk Sn to the nanograined structure. 2) We then observed the fragmentation process of the nanograined structure and subsequent coalescence during desodiation. 3) Using a technique combining classical molecular dynamics (MD) simulations and density functional theory (DFT) calculations, we elucidate the mechanism of the self-assembly behavior of fragmented Sn NPs by analysing the role of electrolytes in promoting the coalescence of fragmented NPs. 4) We

experimentally confirmed that the structural architecture constructed by the self-assembling of pulverized NPs could lead to considerable improvements in the rate performance, capacity, and cyclability of the battery.
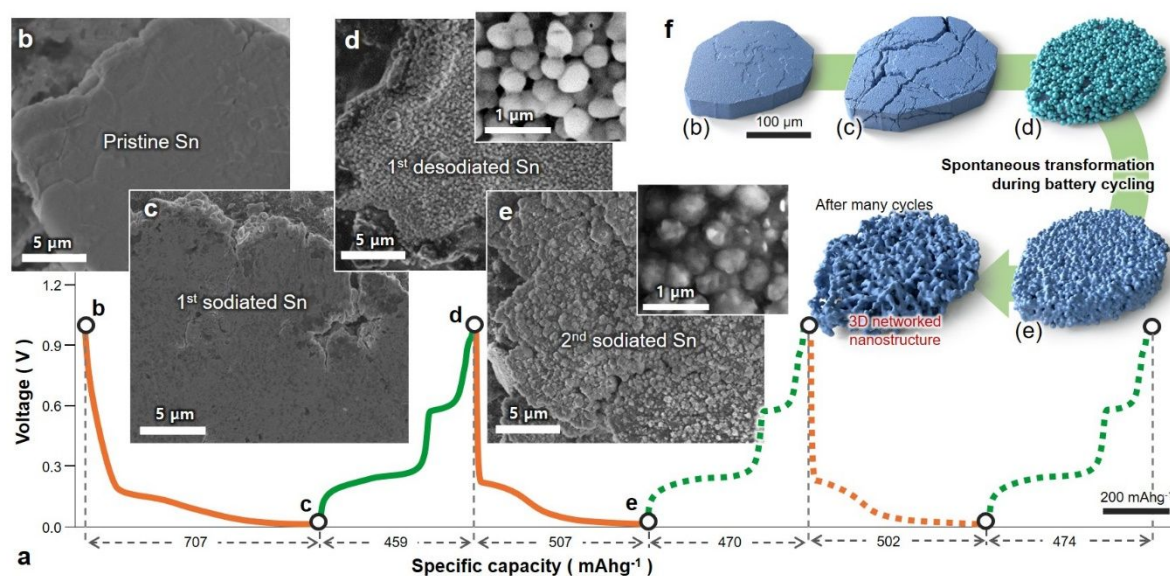

Figure 1. (a) Voltage–capacity curve of the Na–Sn battery measured at a current rate of 15C. Secondary electron images of Sn flakes extracted from the **(b)** uncycled, **(c)** firstly fully discharged (sodiated), **(d)** firstly fully charged (desodiated), and **(e)** secondly fully discharged Na–Sn battery. In the images, only partial sections of the Sn flakes with sizes of ~150 μm are shown. **(f)** Schematic of the structural evolution of a Sn flake during battery cycling.

To explore the structural origins providing the excellent properties of the Na–Sn battery (Figure S1)[16-32], we observed the structural evolution of bulk Sn crystals during battery cycling. For this purpose, we prepared Na–Sn batteries having an electrolyte comprising 1M of $NaPF_6$ dissolved in a dimethoxyethane (DME) solvent (Methods). Four different anode samples were prepared by cycling to different states of charge, as indicated in the

corresponding voltage–capacity curves measured during battery cycling at $15C$ (Figure 1a).

The first sodiation started with a specific capacity of 707 mAhg^{-1}. At this composition, the

crystalline Sn (c-Sn) expands by an average of 300% in volume. The structural change was

confirmed by observing Sn flakes extracted from the pristine (Figure 1b) and firstly sodiated

Na–Sn batteries (Figure 1c). Unlike the unreacted Sn flake, the sodiated Sn exhibits hairline

cracks associated with the volume expansion[33]. During subsequent desodiation, the extraction

of Na$^+$ transforms the initially smooth Sn flake to a structure covered with weakly connected

Sn NPs (Figure 1d). During the second sodiation, the insertion of Na$^+$ transforms Sn NPs to

Na-rich phases (Na$_x$Sn), causing the NPs to expand. The expansion of Sn NPs fills free spaces

between weakly connected Sn NPs, while leaving a bumpy surface of sodiated NPs (Figure

1e). The above observations suggest that the repetition of sodiation and desodiation

progressively transforms the initial morphology of bulk Sn to porous Sn nanostructures (Figure
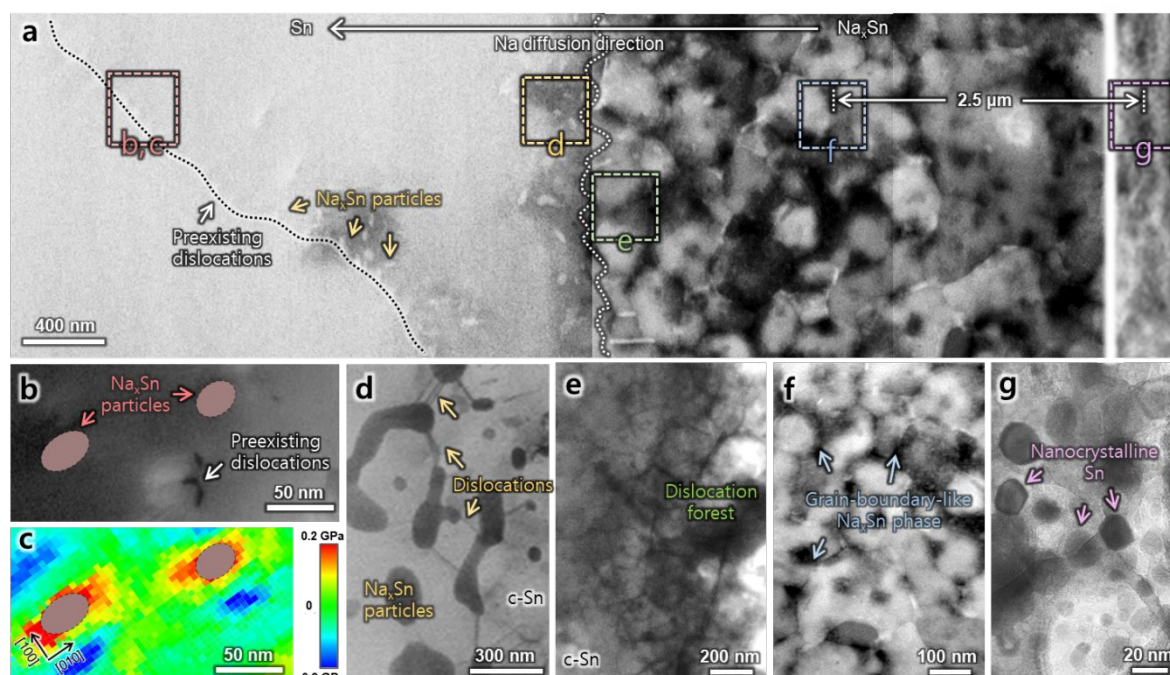
1f).

6 / 23

Figure 2. (a) TEM image of the region near the interface of a partially sodiated Sn obtained by directly contacting a Na lump to a c-Sn flake, which demonstrates the overall sequence of structural evolution associated with sodiation. In the image, Na diffusion proceeds from the right to the left side. **(b)** Magnified image of c-Sn ~2.0 μm away from the interface (white dotted line), which shows Na$_x$Sn NPs dangling on dislocation cores. **(c)** Distribution of stresses measured using PED along the direction of the full dislocation Burgers vector ([100]) of c-Sn. **(d)** Nucleation of new dislocations in the vicinity of the Na$_x$Sn particles. **(e)** Formation of high-density dislocations in c-Sn near Na$_x$Sn particles. **(f)** Sn crystals (bright) surrounded by grain-boundary-like Na$_x$Sn phases (dark). **(g)** Sn NPs (dark) embedded in Na$_x$Sn phases (bright). Note that to clearly reveal Na-rich phases and dislocation structures, the TEM images of (a), (d), and (f) were recorded using the dark field mode, whereas those of (e) and (g) were recorded using the bright field mode.

7 / 23

To analyse the changes in the microstructure of c-Sn during sodiation, we prepared a cross section of a c-Sn flake extracted from a partially sodiated Sn anode. Sodiation proceeded with the formation of a tortuous diffusional interface by leaving the Na-rich phases behind (Figure S2a). However, unlike Si- and Sb-based anodes, in which carrier ions penetrate to depths of 100–300 nm[34, 35], Na$^+$ penetrated c-Sn flakes to depths larger than 2 μm at 15C during the first sodiation. According to energy-dispersive spectroscopy (EDS) analyses, Na was detected even in seemingly unreacted Sn regions away from the interface (Figure S2b). This unusual result is attributed to the characteristic diffusion behavior of Na and can be explained by observing the structural evolution of a partially sodiated Sn flake over a large area (Figure 2a). The unreacted Sn regions, located 2–3 μm ahead of the interface, showed that these regions are characterised by low-density dislocations (red dashed box in Figure 2a). A closer examination of these dislocations reveals NPs dangling on dislocation lines (Figure 2b). The corresponding EDS map shows that these particles are Na$_x$Sn phases (Figure S3). The unique dislocation structure, decorated with Na$_x$Sn particles, suggests that Na diffusion was facilitated by the commonly known "dislocation pipe diffusion". Because the diffusion barrier is considerably lower along the dislocation core than through the lattice, Na$^+$ can migrate two to three orders of magnitude faster along dislocation cores than through the lattice of c-Sn[11, 12]. This explains the existence of Na into the deep interior regions of c-Sn (denoted by the arrows in Figure S2a).

With continued sodiation, additional Na$^+$ is supplied through dislocation cores, which renders Na-rich particles dangling on dislocations to grow and develops residual stresses on their nearside. We evaluated the stresses at regions near Na$_x$Sn particles using the precession electron diffraction (PED) technique[36-38] (see Methods). Figure 2c presents the PED map, showing the distribution of residual stresses measured along the direction of the full dislocation

8 / 23

Burgers vector ([100]) of c-Sn located 2 μm ahead of the propagating interface. Tensile residual stresses are generated near Na_xSn particles and tend to increase with the particle size. With the growth of particles to sizes larger than 30 nm, tensile stresses close to 200 MPa begin to develop near the Na-rich particles (Figure 2c). Such magnitudes of tensile stresses are similar or comparable to the yield strengths (~200 MPa) of nanoscale Sn regions adjacent to the Na-rich particles[39]. This indicates that the nucleation of new dislocations is feasible as the particles grow to sizes larger than 30 nm. Indeed, dislocations are noted to newly nucleate near Na-rich particles with sizes larger than 30 nm (Figure 2d). The growth of these particles expands the area with stresses larger than 200 MPa, which led to a large-scale bursting of dislocations and formation of dislocation cell structures (Figure 2e). Because these dislocations again act as preferential pathways for Na diffusion, the Na accumulation in dislocation cells transforms the Na-rich bulk Sn to nanograined Sn encaged by 3D networked grain-boundary-like Na_xSn phases (the dark phase in Figure 2f). The continued inflow of Na^+ thickens the Na-rich shells by eroding individual Sn crystals to sizes of a few tens of nanometres, and thus transforms bulk Sn crystals to the Na-rich phases embedded with Sn NPs with diameters of 10–20 nm (Figure 2g).
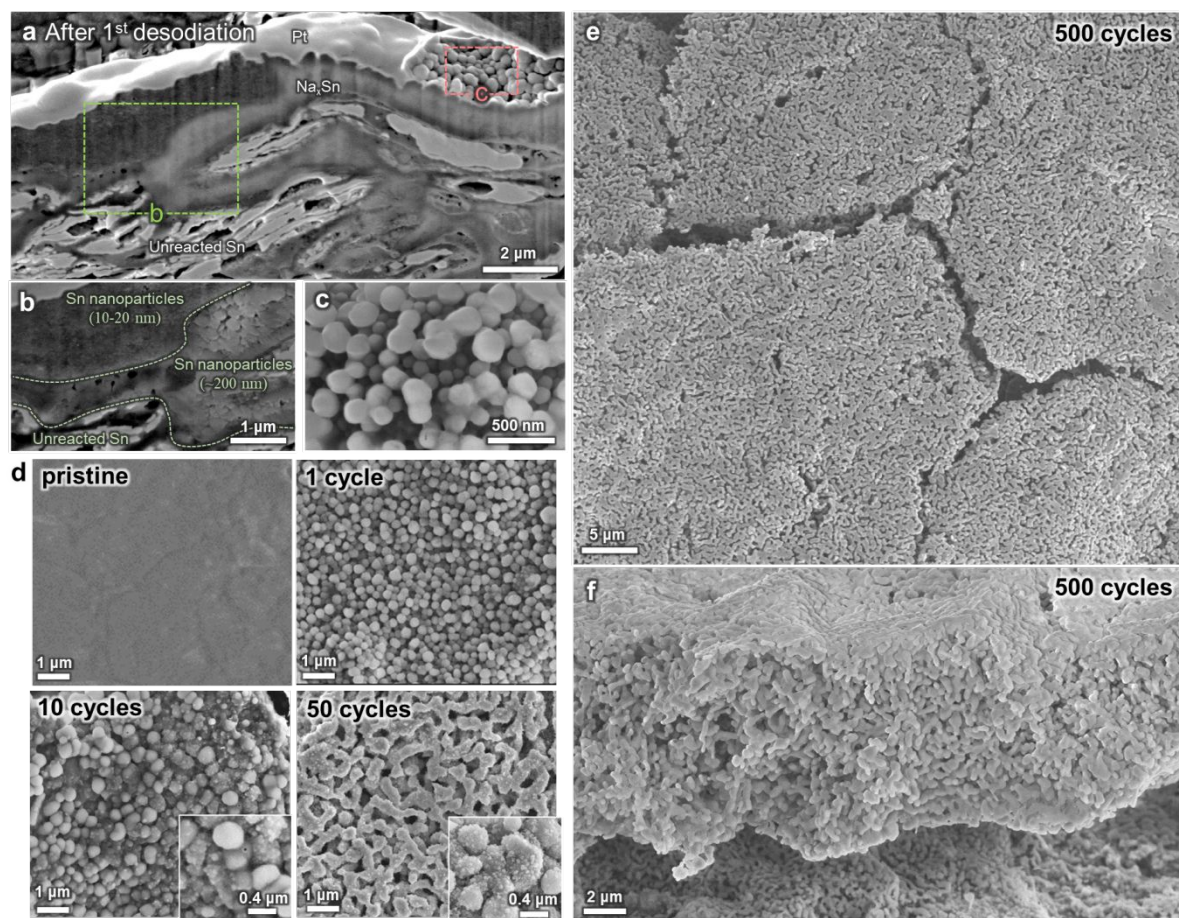
Figure 3. (a) Cross-sectional view of the desodiated Sn flake extracted from the firstly fully charged Na–Sn battery. A protective Pt layer was deposited on the surface of the desodiated Sn flake to prevent structural degradations during the focused-ion beam (FIB) cutting. Magnified images of the (b) interior and (c) surface regions outlined by the rectangles in (a). (d) A series of images of the surfaces of the Sn flakes extracted from the pristine anode and cycled anodes subjected to 1, 10, and 50 cycles, which show the evolution of the bulk Sn to a 3D networked Sn nanostructure constructed with self-assembled Sn NPs. Secondary electron images of the (e) surface and (f) cross-section of the Sn flake extracted from the 500-times-cycled Na-Sn half-cell.

Having elucidated the restructuring of the bulk Sn to the nanograined Na-rich phases during sodiation, we next analyse the transformation of the sodiated bulk Sn into Sn NPs during subsequent desodiation and their self-assembling to porous Sn nanostructures (Figure 1f). For this purpose, we extracted desodiated Sn flakes from the cycled batteries to evaluate the microstructures. Figure 3a shows a cross-sectional view of the desodiated Sn flake subjected to one battery cycle, which reveals various microstructures with a speckled contrast. Although certain regions of the Sn flake remain unreacted (in bright grey), Na^+ have penetrated the Sn flake to a depth greater than ~2 μm during the first battery cycle (in dark grey). Figure 3b shows a magnified image of the region corresponding to rectangle "b" in Figure 3a, suggesting that Sn NPs were formed owing to the extraction of Na from the nanograined Na-rich phases. Another important observation is that individual Sn NPs in the interior region of desodiated Sn flakes are connected by forming weak necks. This partial coalescence is more evident for Sn NPs on the surface of the Sn flake (Figure 3c), showing the surface covered with weakly connected Sn NPs. The examination of the surface shows that the sizes (~200 nm) of the Sn NPs on the surface are considerably larger than those (10–20 nm) in the subsurface region. As Sn NPs at the outer surface of the Sn flake exhibit high surface energy and are in direct contact with the electrolyte, they must have grown by the coalescence of fragmented Sn NPs upon contact with the electrolyte medium.

To further analyse the structural evolution of the Sn flake associated with the additional cycling, we observed the cross sections and surfaces of the desodiated Sn flake subjected to further battery cycles. Compared to the desodiated sample subjected to one cycle (Figure 3a), the desodiated Sn flake subjected to ten cycles did not show unreacted Sn regions (Figure S4). This indicates that, with the repetitive charge–discharge processes, Na penetrated to the entire

11 / 23

volume of the Sn flake. Furthermore, with repetitive sodiation and desodiation, the sequential

pulverization and coalescence gradually transform the bulk Sn to the 3D networked porous Sn

nanostructure (Figure 3d). Such gradual restructuring via the sequential pulverization and

coalescence transforms the entire volume of the initially bulk Sn flake to the 3D networked

porous Sn nanostructure (Figures 3e and 3f).
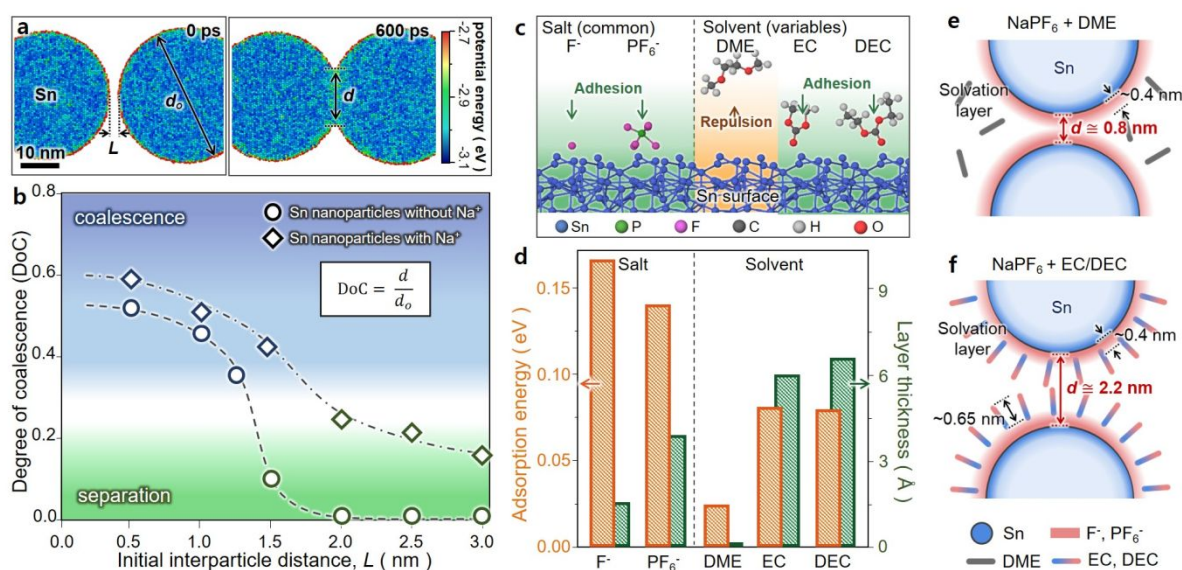
Figure 4. (a) Two representative frames captured during the classical MD simulations, which

show two Sn NPs spontaneously coalescing to reduce their potential energies. **(b)** Variations

in degree of coalescence evaluated for the two Sn NPs as a function of interparticle distance.

(c) Surfaces of the Sn NPs used to replicate the interfacial interactions with various solute ions

(F^-, PF_6^-) and solvents (EC, DEC, and DME) comprising the electrolytes. **(d)** Adsorption

energies calculated for F^-, PF_6^-, EC, DEC, and DME upon interaction with the Sn surface. The

thicknesses of various solvation layers predicted using the stable solvent structures are

superimposed in the graph. Schematics of the Sn NP-electrolyte interfaces formed under

different electrolytes composed of **(e)** $NaPF_6$ in DME and **(f)** $NaPF_6$ in EC/DEC. The colours represent the charge states of the solvation layers (neutral (grey), positive (blue), and negative (red)).

The structural changes of bulk c-Sn discussed in the previous sections (Figures 2 and 3) suggest that the observed structural changes of the bulk c-Sn originated from the pulverization of the bulk Sn and spontaneous coalescence of pulverized Sn NPs in the electrolyte. Although the coalescence of NPs is a well-known phenomenon occurring in various liquid media[40, 41], the pathways towards this behavior are still largely unexplored because this phenomenon not only occurs within a short period of time but also proceeds by the interaction of atomic-scale structural motifs in a liquid medium[41-43]. In this study, we analysed the coalescence behavior of the Sn NPs in the presence of various electrolytes by multi-scale simulations combining classical MD and DFT calculations.

Owing to the high surface-area-to-volume ratio and low melting temperature of the Sn NPs, they tend to coalesce to reduce the surface energy[9]. However, their coalescence is spontaneous and plausible only when the distances between Sn NPs are sufficiently small[8]. We performed large-scale MD simulations to determine the critical spacing, below which spontaneous coalesce occurs between two adjacent Sn NPs (see Methods). Figure 4a shows an example of a MD simulation performed on two 20-nm-diameter bare Sn particles. The particles coalesce when they are separated by less than ~1.5 nm (Figure 4b). However, during the actual battery operation, Sn NPs remain in direct contact with electrolytes comprising various solute ions such as Na^+, F^-, and PF_6^- as well as solvent molecules such as DME. These environments can influence the coalescence behavior of Sn NPs. Firstly, calculations on the effect of Na^+ on

the coalescence behavior of the Sn NPs reveal that the presence of Na^+ promotes the reaction

between the two adjacent Sn NPs, such that they coalesce upon separation by a distance less

than ~3 nm (Figures 4b and S5).

The above results suggest that other ionic components, such as F^-, PF_6^-, and DME

molecules comprising the electrolytes may also affect the propensity for the coalescence of Sn

NPs. Generally, the surfaces of metal NPs dissolved in colloidal solutions are positively

charged[44], and thus attract surrounding negatively charged solute ions and solvent molecules

to form a solvation layer. The so-formed solvation layer separates NPs so that the coalescence

of NPs is more difficult to occur with a thicker solvation layer[45]. Therefore, the effects of

various electrolytes on the coalescence between Sn NPs were evaluated by predicting the

thickness of the solvation layer, conceivably formed by the interaction with solute ions and

solvent molecules comprising the electrolyte.

We performed DFT calculations to analyse the interactions at the surfaces of the Sn

NPs in the presence of various solute ions (F^-, PF_6^-) and solvent molecule (DME) comprising

the electrolyte used in this study (for detailed structures, dimensions, and charge density

distribution of F^-, PF_6^-, and DME, see Figure S6). For comparison, calculations were also

performed for other typical solvent molecules (ethylene carbonate (EC) and diethyl carbonate

(DEC)). For this purpose, we prepared the surface of the Sn NP used to replicate the interfacial

interactions with various solute ions and solvent molecules (Figure 4c). Calculations revealed

that both F^- and PF_6^- solute ions adhere to the Sn surface, while the molecular DME remains

unabsorbed (Figure S7). The adsorption tendencies of various components of the electrolytes

to the Sn NP were quantitatively evaluated by considering their adsorption energies. Both F^-

and PF_6^- ions exhibit large adsorption energies (0.17 and 0.14 eV/atom, respectively), whereas

DME exhibits a markedly small adsorption energy (0.02 eV/atom) (Figure 4d). This comparison explains the presence of the different degrees of adsorption of the various solute ions and solvent molecules, which determines the solvation layer thicknesses adhered to the Sn surface, and thus changes the propensity for the coalescence between Sn NPs. Figure 4d shows the possible thickness of the solvation layer formed on the surface of the Sn NPs estimated by considering the sizes of various types of solute ions and solvent molecules. Both F^- and PF_6^- ions can adsorb on the Sn surface and form layers with thicknesses of 1.5 and 3.8 Å, respectively. However, the DME molecules cannot easily adsorb on Sn NPs and do not contribute to the formation of additional solvation layers. Consequently, the thickness of the solvation layer formed in the presence of the electrolyte comprising $NaPF_6$ and DME is considerably smaller than the critical distance (~3 nm) required for the coalescence of Sn NPs (Figure 4b), which facilitates the coalescence reaction.

Comparative studies were performed to further analyse the adhesion behavior of EC and DEC solvent molecules and their effects on the coalescence of Sn NPs (Figures 4c and d). Calculations show that the adsorption energies of EC and DEC molecules are 0.080 and 0.079 eV/atom, respectively. These results indicate that, compared to DME, the molecular EC and DEC exhibit a greater tendency to adhere to the Sn surface. Thus, they are expected to form solvation layers with a thickness greater than ~7 Å (Figure S7). When the interfacial layer (~3.8 Å) composed of F^- and PF_6^- ions is added to this solvation layer composed of EC/DEC molecules, the interfacial layer becomes even thicker and separates the two Sn NPs by a distance larger than 2.2 nm (Figure 4f). Furthermore, because the surfaces of the solvation layers composed of EC/DEC molecules are negatively charged, the NPs covered with these solvation layers repel each other, which can further increase the interspacing between Sn NPs

in the EC/DEC solvents even greater than the critical distance (3 nm) predicted by the MD

simulations (Figure 4b). This makes the coalescence between Sn NPs in the EC/DEC solvents

unfeasible, which leads to the electrical isolation of pulverized Sn NPs (Figure S8).
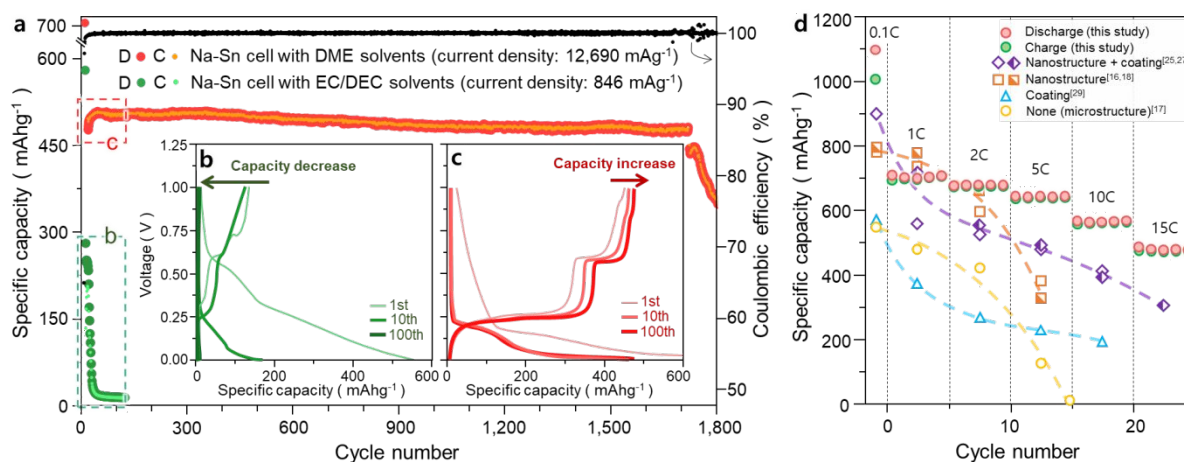

Figure 5. Electrochemical performances of the Na–Sn cell. (a) Capacities and coulombic

efficiency of the Na–Sn half-cells with two different solvents, DME and EC/DEC.

Charging(desodiation) and discharging(sodiation) capacity of half-cells are denoted in the

legend as 'C' and 'D', respectively. Changes in voltage–capacity profiles of the Na–Sn cells

with (b) DME and (c) EC/DEC measured during the initial 100 cycles. (d) Changes in specific

capacity of the Na–Sn half-cell with an electrolyte containing DME as a function of

charge/discharge rate. The specific capacities of Sn anodes modified with various nanoscale

Sn and surface coatings are also shown[16-18, 25, 27, 29].

The effect of the structural change of c-Sn on the actual electrochemical performance

was evaluated for Sn anodes with and without self-assembling capability. For this purpose, we

prepared Na-Sn half-cells containing 1M of $NaPF_6$ dissolved in DME. For comparison, Na–Sn half-cell counterparts containing 1M of $NaPF_6$ dissolved in EC/DEC were also fabricated. Figure 5a shows the changes in specific capacities of the two Na–Sn batteries measured as a function of battery cycle. The Na–Sn half-cell containing the EC/DEC solvent initially exhibits a capacity of <200 $mAhg^{-1}$, which subsequently rapidly decreases with battery cycles even at the slow charging rate of 846 mAg^{-1} (equivalent to 1C) (Figures 5b). The reduction in capacity is attributed to the structural degradation of the Sn anode during repeated cycling. This degradation phenomenon has been extensively analysed for various alloying anodes[3-6]. On the other hand, the Na–Sn half-cell containing the DME solvent exhibits a large capacity of 459 $mAhg^{-1}$ in the first cycle at the charging rate of 12,690 mAg^{-1} (equivalent to 15C) (Figure 5a). Unlike in the case of the Na–Sn cell with EC/DEC, the capacity increased gradually by additional 5–10% (Figures 5a and c) with the increase in battery cycles to 50, which is then maintained during 1,700 cycles. This capacity increase is also observed in a low charge and discharge rate (1C) (Figure S9).

Subsequently, we measured the capacities of the Sn anode with the DME solvent at various C-rates (Figures 5d and S10). For comparison, the capacities of various Sn anodes, based on nanoscale Sn, surface modifications, or combination of the two methods, are also presented[16-18, 25, 27, 29]. Despite the partial improvements in the capacity and cyclic stability, the methods used in previous studies significantly reduced the capacity at C-rates greater than 5. This is because for these batteries utilizing electrolytes containing the EC/DEC solvent, the structural degradation of the Sn anodes is unavoidable, causing the isolation of electrode materials and capacity fading.

Conversely, the Sn anode with the DME solvent exhibited an excellent performance,

17 / 23

even without modifications. The measured properties can be interpreted based on the spontaneous restructuring of the bulk Sn in the appropriate electrolyte and characteristics of the resultant Sn nanostructure The spontaneous restructuring of the bulk Sn enabled physical contacts between the pulverized Sn NPs, which prevents them from electrical isolation and thus increases the anode capacity. Furthermore, the structural evolution transformed the initially bulk Sn into the porous nanostructure. The free space in the porous nanostructure can accommodate the volume expansion of the anode associated with sodiation and thus prevents the accumulation of residual stresses. This not only alleviates the tendency for the self-limiting Na diffusion[46, 47] but also enhances the structural integrity, which leads to improved capacity and cyclic stability of the anode. Because the porous Sn nanostructure is constructed with 200-nm-thick struts composed of Sn NPs, this unique nanostructure is characterised by a short diffusion distance (x) and large surface and grain boundary areas. As the diffusivity (D) is two to three orders of magnitude larger along the surface and grain boundary than along the lattice[11, 12], the Sn nanostructure can rapidly transport Na^+ to the interior of the Sn nanostructure, according to $t \propto x^2/D$ relation[48]. The above characteristics of the porous nanostructure explain how the structure presented in this study can simultaneously improves the contrasting properties of the anode to an unprecedented level. It is also noted from Figure 5a that the capacity of the Na-Sn half-cell containing DME decreases rapidly after 1,700 cycles. In general, battery cycling is always associated with the decomposition reaction of the electrolyte itself and the Na consumption by the formation of solid-electrolyte interfaces and solvation shell on the surface of fragmented Sn NPs[49, 50]. Such reactions at the anode surface cause the depletion of charge carriers and deteriorate electrolyte[51], causing a rapid fading in the capacity by hindering the transportation of Na^+. This is particularly the case for the nanostructured anode with large surface areas, rendering the capacity to quickly fade. For this issue, a more

systematic future study is necessary.

In summary, the structural evolution of the Sn anode occurred spontaneously in the DME-containing electrolyte in the following order, 1) nucleation of high-density dislocations during sodiation, 2) pulverization of bulk Sn during desodiation, and 3) spontaneous coalescence of pulverized Sn NPs in DME-containing electrolyte. The proposed method can be regarded as an alternative robust approach to obtain nanostructured anode in large quantities. Thus, it paves the way for the fabrication of batteries with simultaneously improved electrochemical properties.

Acknowledgements

Author contributions

J.-H.P. and Y.-S.C contributed equally to this work.

Competing interests

The authors declare no competing interests.

Additional information

Supplementary information is available for this paper at https://doi.org/####.

Reprints and permissions information is available at ####.

Correspondence and requests for materials should be addressed to J.-C.L.

References

1. Huggins, R. A., Lithium alloy negative electrodes. *Journal of Power Sources* **1999,** 81, 13-19. DOI: 10.1016/S0378-7753(99)00124-X

2. Tavassol, H.; Jones, E. M.; Sottos, N. R.; Gewirth, A. A., Electrochemical stiffness in lithium-ion batteries. *Nat Mater* **2016,** 15, (11), 1182-1187. DOI: 10.1038/nmat4708

3. Magasinski, A.; Dixon, P.; Hertzberg, B.; Kvit, A.; Ayala, J.; Yushin, G., High-performance lithium-ion anodes using a hierarchical bottom-up approach. *Nat Mater* **2010,** 9, (4), 353-358. DOI: 10.1038/nmat2725

4. Mortazavi, M.; Deng, J.; Shenoy, V. B.; Medhekar, N. V., Elastic softening of alloy negative electrodes for Na-ion batteries. *Journal of power sources* **2013,** 225, 207-214. DOI: 10.1016/j.jpowsour.2012.10.044

5. Kasavajjula, U.; Wang, C.; Appleby, A. J., Nano-and bulk-silicon-based insertion anodes for lithium-ion secondary cells. *Journal of power sources* **2007,** 163, (2), 1003-1039. DOI: 10.1016/j.jpowsour.2006.09.084

6. Li, Y.; Yan, K.; Lee, H.-W.; Lu, Z.; Liu, N.; Cui, Y., Growth of conformal graphene cages on micrometre-sized silicon particles as stable battery anodes. *Nature Energy* **2016,** 1, (2), 1-9. DOI: 10.1038/nenergy.2015.29

7. Shirai, H.; Nguyen, M. T.; Ishida, Y.; Yonezawa, T., A new approach for additive-free room temperature sintering of conductive patterns using polymer-stabilized Sn nanoparticles. *Journal of materials chemistry C* **2016,** 4, (11), 2228-2234. DOI: 10.1039/C6TC00161K

8. Cao, C.; Huang, K.; Shi, J.; Zheng, D.; Wang, W.; Gu, L.; Bai, H., Liquid-like behaviours of metallic glassy nanoparticles at room temperature. *Nat Commun* **2019,** 10, (1), 1-8. DOI: 10.1038/s41467-019-09895-3

9. Yuk, J. M.; Jeong, M.; Kim, S. Y.; Seo, H. K.; Kim, J.; Lee, J. Y., In situ atomic imaging of coalescence of Au nanoparticles on graphene: rotation and grain boundary migration. *Chemical Communications* **2013,** 49, (98), 11479-11481. DOI: 10.1039/C3CC46545D

10. Yuk, J. M.; Park, J.; Ercius, P.; Kim, K.; Hellebusch, D. J.; Crommie, M. F.; Lee, J. Y.; Zettl, A.; Alivisatos, A. P., High-resolution EM of colloidal nanocrystal growth using graphene liquid cells. *Science* **2012,** 336, (6077), 61-64. DOI: 10.1126/science.1217654

11. Swaroop, S.; Kilo, M.; Argirusis, C.; Borchardt, G.; Chokshi, A. H., Lattice and grain boundary diffusion of cations in 3YTZ analyzed using SIMS. *Acta materialia* **2005,** 53, (19), 4975-4985. DOI: 10.1016/j.actamat.2005.05.031

12. Lee, H.-J.; Kim, S.-H.; Lee, J.-C., Promotion of C diffusion to prepare a high-strength wear-resistant Ti alloy. *Scripta Materialia* **2016,** 115, 33-37. DOI: 10.1016/j.scriptamat.2015.12.024

13. Byeon, Y.-W.; Choi, Y.-S.; Ahn, J.-P.; Lee, J.-C., Isotropic Sodiation Behaviors of Ultrafast-Chargeable Tin Crystals. *ACS applied materials & interfaces* **2018,** 10, (48), 41389-41397. DOI: 10.1021/acsami.8b15758

14. Huang, J. Y.; Zhong, L.; Wang, C. M.; Sullivan, J. P.; Xu, W.; Zhang, L. Q.; Mao, S. X.; Hudak, N. S.; Liu, X. H.; Subramanian, A., In situ observation of the electrochemical lithiation of a single SnO2 nanowire electrode. *Science* **2010,** 330, (6010), 1515-1520. DOI: 10.1126/science.1195628

15. Kim, C.; Kim, I.; Kim, H.; Sadan, M. K.; Yeo, H.; Cho, G.; Ahn, J.; Ahn, J.; Ahn, H., A self-healing Sn anode with an ultra-long cycle life for sodium-ion batteries. *Journal of Materials Chemistry A* **2018,** 6, (45), 22809-22818. DOI: 10.1039/C8TA09544B

16. Nam, D.-H.; Kim, T.-H.; Hong, K.-S.; Kwon, H.-S., Template-free electrochemical synthesis of Sn nanofibers as high-performance anode materials for Na-ion batteries. *Acs Nano* **2014,** 8, (11), 11824-11835. DOI: 10.1021/nn505536t

17. Zhang, B.; Rousse, G.; Foix, D.; Dugas, R.; Corte, D. A. D.; Tarascon, J. M., Microsized Sn as advanced anodes in glyme-based electrolyte for Na-Ion batteries. *Advanced Materials* **2016,** 28, (44), 9824-9830. DOI: 10.1002/adma.201603212

18. Kim, T.-H.; Hong, K.-S.; Sohn, D.; Kim, M.; Nam, D.-H.; Cho, E.; Kwon, H., One-step synthesis of multilayered 2D Sn nanodendrites as a high-performance anode material for Na-ion batteries. *Journal of Materials Chemistry A* **2017,** 5, (38), 20304-20315. DOI: 10.1039/C7TA06469A

19. Han, X.; Liu, Y.; Jia, Z.; Chen, Y.-C.; Wan, J.; Weadock, N.; Gaskell, K. J.; Li, T.; Hu, L., Atomic-layer-deposition oxide nanoglue for sodium ion batteries. *Nano Lett* **2014,** 14, (1), 139-147. DOI: 10.1021/nl4035626

20. Fukunishi, M.; Yabuuchi, N.; Dahbi, M.; Son, J.-Y.; Cui, Y.; Oji, H.; Komaba, S., Impact of the Cut-Off Voltage on Cyclability and Passive Interphase of Sn-Polyacrylate Composite Electrodes for Sodium-Ion Batteries. *The Journal of Physical Chemistry C* **2016,** 120, (28), 15017-15026. DOI: 10.1021/acs.jpcc.6b03459

21. Dai, K.; Zhao, H.; Wang, Z.; Song, X.; Battaglia, V.; Liu, G., Toward high specific capacity and high cycling stability of pure tin nanoparticles with conductive polymer binder for sodium ion batteries. *Journal of Power Sources* **2014,** 263, 276-279. DOI: 10.1016/j.jpowsour.2014.04.012

22. Nam, D.-H.; Hong, K.-S.; Lim, S.-J.; Kim, T.-H.; Kwon, H.-S., Electrochemical properties of electrodeposited Sn anodes for Na-ion batteries. *The Journal of Physical Chemistry C* **2014,** 118, (35), 20086-20093. DOI: 10.1021/jp504055j

23. Kim, C.; Lee, K.-Y.; Kim, I.; Park, J.; Cho, G.; Kim, K.-W.; Ahn, J.-H.; Ahn, H.-J., Long-term cycling stability of porous Sn anode for sodium-ion batteries. *Journal of Power Sources* **2016,** 317, 153-158. DOI: 10.1016/j.jpowsour.2016.03.060

24. Komaba, S.; Matsuura, Y.; Ishikawa, T.; Yabuuchi, N.; Murata, W.; Kuze, S., Redox reaction of Sn-polyacrylate electrodes in aprotic Na cell. *Electrochemistry Communications* **2012,** 21, 65-68. DOI: 10.1016/j.elecom.2012.05.017

25. Liu, Y.; Zhang, N.; Jiao, L.; Chen, J., Tin nanodots encapsulated in porous nitrogen-doped carbon nanofibers as a free-standing anode for advanced sodium-ion batteries. *Advanced Materials* **2015,** 27, (42), 6702-6707. DOI: 10.1002/adma.201503015

26. Liu, Y.; Zhang, N.; Jiao, L.; Tao, Z.; Chen, J., Ultrasmall Sn nanoparticles embedded in carbon as high-performance anode for sodium-ion batteries. *Advanced Functional Materials* **2015,** 25, (2), 214-220. DOI: 10.1002/adfm.201402943

27. Luo, B.; Qiu, T.; Ye, D.; Wang, L.; Zhi, L., Tin nanoparticles encapsulated in graphene backboned carbonaceous foams as high-performance anodes for lithium-ion and sodium-ion storage. *Nano Energy* **2016,** 22, 232-240. DOI: 10.1016/j.nanoen.2016.02.024

28. Liu, Y.; Xu, Y.; Zhu, Y.; Culver, J. N.; Lundgren, C. A.; Xu, K.; Wang, C., Tin-coated viral nanoforests as sodium-ion battery anodes. *Acs Nano* **2013,** 7, (4), 3627-3634. DOI: 10.1021/nn400601y

29. Jeon, Y.; Han, X.; Fu, K.; Dai, J.; Kim, J. H.; Hu, L.; Song, T.; Paik, U., Flash-induced reduced graphene oxide as a Sn anode host for high performance sodium ion batteries. *Journal of Materials Chemistry A* **2016,** 4, (47), 18306-18313. DOI: 10.1039/C6TA07582G

30. Sha, M.; Zhang, H.; Nie, Y.; Nie, K.; Lv, X.; Sun, N.; Xie, X.; Ma, Y.; Sun, X., Sn nanoparticles@ nitrogen-doped carbon nanofiber composites as high-performance anodes for sodium-ion batteries. *Journal of Materials Chemistry A* **2017,** 5, (13), 6277-6283. DOI: 10.1039/C7TA00690J

31. Chen, S.; Ao, Z.; Sun, B.; Xie, X.; Wang, G., Porous carbon nanocages encapsulated with tin nanoparticles for high performance sodium-ion batteries. *Energy Storage Materials* **2016,** 5, 180-190. DOI: 10.1016/j.ensm.2016.07.001

32. Sadan, M. K.; Choi, S.-H.; Kim, H. H.; Kim, C.; Cho, G.-B.; Kim, K.-W.; Reddy, N.; Ahn, J.-H.; Ahn, H.-J., Effect of sodium salts on the cycling performance of tin anode in sodium ion batteries. *Ionics* **2018,** 24, (3), 753-761. DOI: 10.1007/s11581-017-2243-2

33. Choi, Y.-S.; Byeon, Y.-W.; Ahn, J.-P.; Lee, J.-C., Formation of Zintl ions and their configurational change during sodiation in Na–Sn battery. *Nano Lett* **2017,** 17, (2), 679-686. DOI: 10.1021/acs.nanolett.6b03690

34. Choi, Y.-S.; Park, J.-H.; Ahn, J.-P.; Lee, J.-C., Anisotropic Swelling Governed by Orientation-

Dependent Interfacial Na Diffusion in Single-Crystalline Sb. *Chemistry of Materials* **2019**. DOI: 10.1021/acs.chemmater.8b05099

35. Liu, X. H.; Fan, F.; Yang, H.; Zhang, S.; Huang, J. Y.; Zhu, T., Self-limiting lithiation in silicon nanowires. *Acs Nano* **2013,** 7, (2), 1495-1503. DOI: 10.1021/nn305282d

36. Vincent, R.; Midgley, P., Double conical beam-rocking system for measurement of integrated electron diffraction intensities. *Ultramicroscopy* **1994,** 53, (3), 271-282. DOI: 10.1016/0304-3991(94)90039-6

37. Favia, P.; Gonzales, M. B.; Simoen, E.; Verheyen, P.; Klenov, D.; Bender, H., Nanobeam diffraction: Technique evaluation and strain measurement on complementary metal oxide semiconductor devices. *J Electrochem Soc* **2011,** 158, (4), H438. DOI: 10.1149/1.3546851

38. Rauch, E. F.; Portillo, J.; Nicolopoulos, S.; Bultreys, D.; Rouvimov, S.; Moeck, P., Automated nanocrystal orientation and phase mapping in the transmission electron microscope on the basis of precession electron diffraction. *Zeitschrift für Kristallographie International journal for structural, physical, and chemical aspects of crystalline materials* **2010,** 225, (2-3), 103-109. DOI: 10.1524/zkri.2010.1205

39. Burek, M. J.; Budiman, A. S.; Jahed, Z.; Tamura, N.; Kunz, M.; Jin, S.; Han, S. M. J.; Lee, G.; Zamecnik, C.; Tsui, T. Y., Fabrication, microstructure, and mechanical properties of tin nanostructures. *Materials Science and Engineering: A* **2011,** 528, (18), 5822-5832. DOI: 10.1016/j.msea.2011.04.019

40. Liao, H.-G.; Cui, L.; Whitelam, S.; Zheng, H., Real-time imaging of Pt3Fe nanorod growth in solution. *science* **2012,** 336, (6084), 1011-1014. DOI: 10.1126/science.1219185

41. Baumgartner, J.; Dey, A.; Bomans, P. H.; Le Coadou, C.; Fratzl, P.; Sommerdijk, N. A.; Faivre, D., Nucleation and growth of magnetite from solution. *Nat Mater* **2013,** 12, (4), 310-314. DOI: 10.1038/nmat3558

42. Nielsen, M. H.; Li, D.; Zhang, H.; Aloni, S.; Han, T. Y.-J.; Frandsen, C.; Seto, J.; Banfield, J. F.; Cölfen, H.; De Yoreo, J. J., Investigating processes of nanocrystal formation and transformation via liquid cell TEM. *Microscopy and Microanalysis* **2014,** 20, (2), 425-436. DOI: 10.1017/S1431927614000294

43. Keller, D.; Henninen, T. R.; Erni, R., Formation of gold nanoparticles in a free-standing ionic liquid triggered by heat and electron irradiation. *Micron* **2019,** 117, 16-21. DOI: 10.1016/j.micron.2018.10.008

44. Abbas, Z.; Labbez, C.; Nordholm, S.; Ahlberg, E., Size-dependent surface charging of nanoparticles. *The Journal of Physical Chemistry C* **2008,** 112, (15), 5715-5723. DOI: 10.1021/jp709667u

45. Xiao, A. W.; Lee, H. J.; Capone, I.; Robertson, A.; Wi, T.-U.; Fawdon, J.; Wheeler, S.; Lee, H.-W.; Grobert, N.; Pasta, M., Understanding the conversion mechanism and performance of monodisperse FeF 2 nanocrystal cathodes. *Nat Mater* **2020**, 1-11. DOI: 10.1038/s41563-020-0621-z

46. Park, J.-H.; Choi, Y.-S.; Byeon, Y.-W.; Ahn, J.-P.; Lee, J.-C., Diffusion kinetics governing the diffusivity and diffusion anisotropy of alloying anodes in Na-ion batteries. *Nano Energy* **2019,** 65, 104041. DOI: 10.1016/j.nanoen.2019.104041

47. Choi, Y.-S.; Byeon, Y.-W.; Park, J.-H.; Seo, J.-H.; Ahn, J.-P.; Lee, J.-C., Ultrafast Sodiation of Single-Crystalline Sn Anodes. *ACS applied materials & interfaces* **2017,** 10, (1), 560-568. DOI: 10.1021/acsami.7b14680

48. Kim, D.; Zhang, K.; Cho, M.; Kang, Y.-M., Critical design factors for kinetically favorable P-based compounds toward alloying with Na ions for high-power sodium-ion batteries. *Energy & Environmental Science* **2019,** 12, (4), 1326-1333. DOI: 10.1039/C9EE00283A

49. Chen, S.; Niu, C.; Lee, H.; Li, Q.; Yu, L.; Xu, W.; Zhang, J.-G.; Dufek, E. J.; Whittingham, M. S.; Meng, S., Critical parameters for evaluating coin cells and pouch cells of rechargeable Li-metal batteries. *Joule* **2019,** 3, (4), 1094-1105. DOI: 10.1016/j.joule.2019.02.004

50. Günter, F. J.; Burgstaller, C.; Konwitschny, F.; Reinhart, G., Influence of the Electrolyte Quantity

on Lithium-Ion Cells. *Journal of The Electrochemical Society* **2019,** 166, (10), A1709. DOI: 10.1149/2.0121910jes

51. Park, J.-H.; Choi, Y.-S.; Lee, H.-J.; Shim, H.-C.; Ahn, J.-P.; Lee, J.-C., Direct-Contact Microelectrical Measurement of the Electrical Resistivity of a Solid Electrolyte Interface. *Nano letters* **2019,** 19, (6), 3692-3698. DOI: 10.1021/acs.nanolett.9b00765

23 / 23